Three-Dimensional Path Planning for Virtual Bronchoscopy

A. P. Kiraly, J. P. Helferty, *Member, IEEE*, E. A. Hoffman, G. McLennan, and W. E. Higgins*, *Fellow, IEEE*

***Abstract*—Multidetector computed-tomography (MDCT) scanners provide large high-resolution three-dimensional (3-D) images of the chest. MDCT scanning, when used in tandem with bronchoscopy, provides a state-of-the-art approach for lung-cancer assessment. We have been building and validating a lung-cancer assessment system, which enables virtual-bronchoscopic 3-D MDCT image analysis and follow-on image-guided bronchoscopy. A suitable path planning method is needed, however, for using this system. We describe a rapid, robust method for computing a set of 3-D airway-tree paths from MDCT images. The method first defines the skeleton of a given segmented 3-D chest image and then performs a multistage refinement of the skeleton to arrive at a final tree structure. The tree consists of a series of paths and branch structural data, suitable for quantitative airway analysis and smooth virtual navigation. A comparison of the method to a previously devised path-planning approach, using a set of human MDCT images, illustrates the efficacy of the method. Results are also presented for human lung-cancer assessment and the guidance of bronchoscopy.**

***Index Terms*—Centerline analysis, CT bronchography, CT imaging, image-guided surgery, path planning, pulmonary imaging, virtual bronchoscopy, virtual endoscopy, 3-D imaging.**

I. Introduction

MODERN multidetector computed-tomography (MDCT) scanners provide large high-resolution three-dimensional (3-D) images of the chest [1], [2]. MDCT scanning, when used in tandem with bronchoscopy, provides a state-of-the-art approach for lung-cancer assessment [3]–[5]. We have been building and validating a lung-cancer assessment system, which enables 3-D MDCT image analysis and follow-on image-guided bronchoscopy [6], [7]. A major component of this system is a method for computing the central airway paths (centerlines) from a 3-D MDCT chest image. This paper describes the method and illustrates the method's use for the planning and guidance of bronchoscopy.

Manuscript received October 16, 2003; revised April 8, 2004. This work was supported in part by the National Instiututes of Health (NIH) under Grant CA-74 325 and Grant CA-91 534 from the National Cancer Institute, in part by the NIH under Grant RR11800, in part by the Olympus Corporation, in part by the Whitaker Foundation, and in part by an NIH Biomedical Research Partnership (NIH-HL-064 368). The Associate Editor responsible for coordinating the review of this paper and recommending its publication was R. M. Summers. *Asterisk indicates corresponding author.*

A. P. Kiraly is with Siemens Corporate Research, Princeton, NJ 08540 USA.

J. P. Helferty is with Lockheed-Martin, King of Prussia, PA 19406 USA.

E. A. Hoffman and G. McLennan are with the College of Medicine, University of Iowa, Iowa City, IA 52242 USA.

*W. E. Higgins is with the Departments of Electrical Engineering, Computer Science and Engineering, and Bioengineering, Pennsylvania State University, University Park, PA 16802, USA and also with the College of Medicine, University of Iowa, Iowa City, IA 52242 USA (e-mail: weh2@psu.edu).

Digital Object Identifier 10.1109/TMI.2004.829332

Recently, a methodology referred to as virtual endoscopy—or virtual bronchoscopy when applied to the chest—has been put forth as a means for assessing large high-resolution 3-D CT chest images [1], [3]–[5], [8]–[21]. In its most basic form, virtual bronchoscopy (VB) is a computer-based approach for "navigating virtually" through airways captured in a 3-D MDCT image. The graphical views generated during VB navigation resemble the endoluminal video views generated by a real bronchoscope. The advantage of VB is that airway analysis can be done noninvasively, thus enabling more careful assessment and follow-on procedure planning. When this basic navigation is supplemented with other viewing tools, such as multiplanar reformatted sections, projections, and thin slabs, the physician gets a multi-faceted graphical view for assessing the chest anatomy [11], [12], [22].

VB techniques are well-suited for the planning and guidance of bronchoscopy. But to use them effectively, a detailed definition of the 3-D airway-tree structure is required. The early research efforts that applied VB to the planning and guidance of bronchoscopy did not use predefined airway paths; during a procedure, the bronchoscopist had to mentally match derived VB views to bronchoscopic video views [3]–[5]. This limits the number of airway sites that can be considered during a procedure, does not entail true direct image guidance (thus reducing accuracy) and, in general, greatly limits the potential of MDCT-guided bronchoscopy. With a detailed axial path structure of the airway tree, more exhaustive planning of bronchoscopy can be accomplished. More sites of interest can be predefined. Also, as demonstrated in Section III.B and discussed in a companion paper [7], the paths can be used for direct MDCT-guidance of live bronchoscopy, alleviating the physician's burden of matching the bronchoscope's position to precomputed VB views.

Hundreds of separate airway branches, following complex 3-D paths, can appear in a typical MDCT chest image. Since manual definition would require an impractical amount of human interaction, a semi-automatic method is necessary for defining this information. A suitable method must: 1) provide a detailed, smooth structure of the airway tree's central axes; 2) require little human interaction; 3) function over a wide range of conditions as observed in typical lung-cancer patients, such as lung-volume variations and unpredictable differences in airway-tree structure brought on by encroaching cancer lesions. Our proposed method meets these requirements. Smooth branches are needed for comfortable navigation through the airways and for more continuous local airway measurements. Some human interaction is acceptable, provided that it fits comfortably within the clinical workflow of MDCT analysis

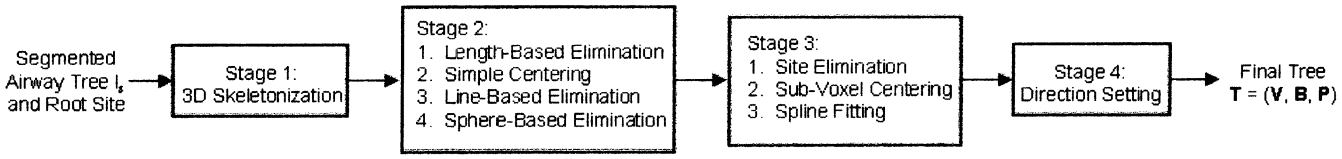

Fig. 1. Block diagram of proposed path-planning method.

and bronchoscopy. Finally, in addition to navigation, which is used in planning and guiding bronchoscopic biopsies, we also wish to make local measurements on airway branches, which is useful for planning bronchoscopy at obstructed sites. Sections II–III will say more on these points.

Before reviewing previously proposed path-planning methods, we first point out that no existing method meets all of our requirements. Our method, specifically tailored to the scenario of the planning and guidance of bronchoscopy, however, does employ concepts from previously proposed methods, in addition to incorporating a few additional ideas. We emphasize that other integrated methods, which might include ideas from the cited literature, are possible. With this said, three general path-planning approaches, which have been applied to angiography, micro-CT imaging, colonoscopy, neurosurgery, liver surgery, and airway analysis, have been proposed previously: 1) branch following [19], [23]–[26]; 2) skeleton-based techniques [27]–[31]; 3) front analysis [32]–[39]. A few other methods, which do not fit into one of these three classes, either rely on labeled data or on a combination of the above techniques [40], [41].

Branch following methods begin at the proximal (root) end of the tree and trace their way through the structure to define a smooth set of paths through the tree. As demonstrated in Section III, these methods can fail to give many paths or give misleading results when the structure exhibits an abrupt size change or asymmetry [19], [23]. Unlike branch following, which progressively analyzes small local portions of data to build up a path or set of paths, skeleton-based techniques first compute a digital skeleton of the entire tree. The skeleton does not give a smooth path structure, but a few of skeleton-based methods do employ post processing to arrive at a set of smooth paths. Finally, front-analysis techniques analyze the properties of an evolving structure, created by region growing or other distance-based methods, to determine path sites and branch points. Centerline methods have been devised specifically for virtual colonography, but these techniques typically produce only one path and are not geared toward tree-like structures (e.g., [27]). Other issues in applying previously proposed methods to VB-based airway-tree analysis and to the planning and guidance of bronchoscopy include: 1) failure to provide visually smooth navigation paths [23]–[26], [28], [30]–[34], [36], [37], [40], [41]; 2) path points are comprised of integer-based coordinates, rendering them unsuitable for detailed navigation [28]–[30]; 3) excessive user input if many branches need to be defined [19], [23], [25]–[28], [31], [35], [37], [40]. We point out again, though, that the underlying ideas of many of the previous approaches could be successfully integrated into a method suitable for our needs, provided that the issues are addressed.

Our proposed method, detailed in Section II, first defines the skeleton of a given segmented 3-D digital MDCT chest image and then performs a multistage refinement of the skeleton to arrive at a final tree structure. The tree consists of a series of paths and branch structural data, suitable for the quantitative planning and live guidance of bronchoscopy. Section III gives performance results and provides applications to VB-based planning and guidance of bronchoscopy. Finally, Section IV offers concluding comments.

II. Method

A. Method Overview and Notation

Fig. 1 depicts a block diagram of the proposed method. A presegmented 3-D image I_s, containing a branching tree structure of interest, and a preselected *root site* denoting the approximate starting location of the tree, serve as inputs. The goal is to produce a description of the tree's branch structure suitable for navigation and quantitative analysis. A tree's branch structure (henceforth referred to as a *tree*) is stored in a data structure given by $\mathbf{T} = (\mathbf{V}, \mathbf{B}, \mathbf{P})$, where $\mathbf{V} = \{\mathbf{v}_1, \ldots, \mathbf{v}_L\}$ is the set of *viewing sites*, $\mathbf{B} = \{\mathbf{b}_1, \ldots, \mathbf{b}_M\}$ is the set of *branches*, $\mathbf{P} = \{\mathbf{p}_1, \ldots, \mathbf{p}_N\}$ is the set of all possible *paths* originating from the root site, and L, M, and N are integers ≥ 1 [19].

A viewing site $\mathbf{v} = (\mathbf{x}, \mathbf{d})$ specifies a single discrete point within the tree, where $\mathbf{x}$ is the *3-D location* (x, y, z) of $\mathbf{v}$ within I_s and $\mathbf{d}$ specifies a *direction vector*. The quantity $\mathbf{d}$ is a quaternion vector of the form (X, Y, Z, W); the quaternion implicitly contains the *viewing direction* and also an up vector that specifies the observer's orientation when viewing the scene from viewing site $\mathbf{v}$ [27], [42], [43].

A branch $\mathbf{b} = \{\mathbf{v}_a \cdots \mathbf{v}_l\}$ consists of an ordered set of connected viewing sites $\mathbf{v}_a, \mathbf{v}_b, \ldots, \mathbf{v}_l \in \mathbf{V}$. With the exception of $\mathbf{b}_1$ (the root branch of the tree), the viewing site $\mathbf{v}_a$ of $\mathbf{b}$ must be a branch (bifurcation) point, while $\mathbf{v}_l$ must be either a branch point or an end point. The last viewing site $\mathbf{v}_l$ of a branch $\mathbf{b}$ will often be given the special designation $l_{\mathbf{b}}$. For a particular branch $\mathbf{b}$, we will sometimes refer to its constituent viewing sites as the sequence $\mathbf{b}(1), \mathbf{b}(2), \mathbf{b}(3)$, etc. If $\mathbf{b}$ is not a terminal branch (i.e., $l_{\mathbf{b}}$ is not an end point), then $\mathbf{b}$ spawns child branches and $l_{\mathbf{b}}$ is a branch point.

Finally, regarding path set $\mathbf{P}$, a path $\mathbf{p} = \{\mathbf{b}_1 \cdots \mathbf{b}_m\}$ consists of an ordered subset of connected branches $\mathbf{b}_1, \ldots, \mathbf{b}_m \in \mathbf{B}$, terminated by two branches, $\mathbf{b}_1$ and $\mathbf{b}_m$, having end points. All paths $\mathbf{p}$ must start with the root branch $\mathbf{b}_1$ and end with a terminal branch. Thus, a path defines a complete traversal through the tree from the root to a terminal branch. $\mathbf{P}$ contains all such paths.

The complete method consists of four separate stages, as shown in Fig. 1. Stage One computes a 3-D skeleton of the presegmented image I_s, where, for our efforts, I_s is computed

using the heavily validated 3-D airway-tree segmentation method of [20]. The skeleton gives an initial estimate of the tree structure $\mathbf{T}$. The subsequent three stages amend this estimate to achieve the final tree $\mathbf{T}$. Stage Two consists of four operations that eliminate false branches and perform an initial voxel-based location adjustment of the remaining branches. Stage Three applies three refining operations that result in a smooth sub-voxel-interpolated tree description. Finally, Stage Four derives viewing directions for each viewing site. Section II-B gives details on the complete method, while Section II-C discusses implementation aspects.

B. Method Details

Stage 1—3-D Skeletonization: The method begins by computing the 3-D skeleton of I_s. In principle, the 3-D skeletonization algorithm must preserve homotopy and not excessively erode the tree geometry; i.e., the algorithm should preserve end points and give skeletal branches for significant branches of the tree. For this paper, we have devised a method that combines the simple-point definition of Saha *et al.* for homotopy preservation and the end-point definition method of Zhou and Toga for geometry preservation [44]–[46]. The method of Saha *et al.*, while rigorously defined, can produce many extraneous short branches and has an embedded surface-detection step that can be very computationally intense [44], [45]. Zhou and Toga's method, while specifically tailored to tree-like structures, gives inaccurate branch-point localization [47]. Our hybrid method combines the strengths of the two approaches for skeletonizing trees.

The first step involves computing two distance metrics, based on the $\langle 1,2,3\rangle$ and $\langle 3,4,5\rangle$ chamfer distance metrics, for all voxels contained in the segmented image I_s [48]. These metrics give each voxel's distance from the tree's predefined root site and outer boundary, respectively. The reasons for using two different chamfer distance metrics are as follows. The $\langle 3,4,5\rangle$ metric more accurately approximates the true Euclidean distance metric. Hence, subtleties on the surface of the segmentation are more likely to produce voxel clusters that become branches in the final skeleton (see below). The $\langle 1,2,3\rangle$ metric, on the other hand, is less sensitive to surface irregularities. But this sensitivity is not needed for measuring distance between two sites, and the metric requires less computation. Next, clusters are formed from 26-connected voxels having the same root-site distance. Clusters having a locally maximal distance from the root site are then further processed. For each such cluster, the voxel furthest from the outer boundary is specially labeled as an end point and never deleted by the remaining operations of this stage. In the event that two or more voxels within a cluster have the same maximum distance from the outer boundary, the voxel that is closest to the cluster's centroid is chosen. These labeled voxels designate end points that are best centered within the tree.

The next part of the method applies an iterative thinning procedure to successive layers of unlabeled voxels. The first candidate layer is comprised of voxels a distance $d = 0$ from the boundary. Following the voxel characterization criteria of Saha *et al.*, simple S-open voxels that are not labeled as end points are candidates for deletion. S-open voxels are those that are 6-connected to the image background at the beginning of the current iteration, and a simple voxel is one that can be deleted from I_s without changing I_s's homotopy [44]. Thinning iterates through standard North, South, East, West, Top, and Bottom scans for voxel deletion until no further simple S-open voxels can be deleted ([49] is one of many 3-D skeletonization algorithms using this scanning technique). The next thinning iteration considers the layer of voxels a distance $d = 1$ from the boundary. This process continues for $d = 2,3,\ldots$, until all layers have been considered. The final result is a 26-connected unit-thick skeleton of the tree. Such scanning, standard in many 3-D thinning algorithms, tries to consider voxels so that directionally unbiased deletion occurs. In reality, however, because the data is discrete, the final skeleton will exhibit some local deviations from the ideal central axial structure. Subsequent stages of our method will attempt to better center these data.

The discrete nature of the data makes it difficult to prove and, indeed, define the geometrical accuracy of a 3-D skeletonization algorithm. For 3-D tree analysis, this is a topic of current research [50]–[52]. Our primary goal is to have a 3-D skeletonization method that robustly defines the airway-tree branches for the first several generations, without exhibiting too many "distracting" extra branches.

Once the raw skeleton is computed, it is stored in the tree data structure $\mathbf{T} = \{\mathbf{V}, \mathbf{B}, \mathbf{P}\}$. Each skeleton voxel defines an initial 3-D location $\mathbf{x}$ for a viewing site $\mathbf{v}$. The conversion of the skeleton to $\mathbf{T}$ starts at the voxel closest to the predefined root site and follows its 26-connected neighbors to define the root branch $\mathbf{b}_1$. If an encountered voxel has only two neighbors, it is stored as a viewing site in $\mathbf{V}$ and added to branch $\mathbf{b}_1$. Otherwise, if it has three or more neighbors, the voxel is a branch point and it begins (two or more) new branches, $\mathbf{b}_2$ and $\mathbf{b}_3$. This process continues for the new branches until the entire skeleton has been processed. Note that the skeleton might contain loops. If a loop is encountered, it is broken into terminal branches. For this circumstance, two cases are possible. In case one, a certain branch point may connect to a previously encountered branch point of upper generation branches that have already been defined. The branch point that completes the loop is deleted. In case two, a branch point might connect to branches yet to be defined, but that eventually form a loop. As these branches become defined, then some voxel will be encountered as in the first case and be deleted. Note that the direction vectors $\mathbf{d}$ for viewing sites $\mathbf{v}$ are not computed until Stage 4.

Finally, given the branch set $\mathbf{B}$, the path set $\mathbf{P}$ is computed. In the structure $\mathbf{T}$, subsequent processing, which will delete or move viewing sites, will not change the tree's basic homotopy, except to delete unwanted branches and better center the viewing sites.

Stage 2—False Branch Elimination and Simple Centering: The main purpose of Stage 2 is to eliminate many of the false branches typically contained in the skeleton produced by Stage 1. Also, the skeletal branches are often not well centered relative to the tree's significant tubular components. The four steps comprising Stage 2 eliminate many of the false branches and begin the branch-centering process. During each step, the tree $\mathbf{T}$ is updated. Intuitively, we define a false branch

as one that is too small geometrically to contain useful information or that arises because of discrete-sampling artifacts. Stage 2 proposes several geometric tests for detecting false branches. We emphasize that alternative operations are possible, but we have found our proposed methods to be effective.

a) Length-based elimination: This step eliminates relatively short terminal branches that are most likely due to insufficient data resolution. A terminal branch is eliminated if it does not extend a sufficient length beyond a sphere inscribed about its parent branch point. Such branches are deemed to have insufficient geometric support to be significant. Two criteria are proposed to identify such branches. Any terminal branch $\mathbf{b}$ that satisfies either of the following criteria is eliminated

$$L_{\mathbf{b}} - S_R(l_{\mathbf{b}_P}) \leq 1 \tag{1}$$

$$\frac{L_{\mathbf{b}} - S_R(l_{\mathbf{b}_P})}{S_R(l_{\mathbf{b}_P})} < 1 \tag{2}$$

where $L_{\mathbf{b}}$ is the length of a branch $\mathbf{b}$, measured as the sum of the distances between consecutive branch viewing sites, $\mathbf{b}_P$ represents the parent branch of $\mathbf{b}$, $l_{\mathbf{b}_P}$ is the last viewing site of $\mathbf{b}_P$, and $S_R(\mathbf{v})$ is the radius of the maximally inscribable sphere, centered at a viewing site $\mathbf{v} = \{\mathbf{x}, \mathbf{d}\}$, which stays within the segmented tree I_s

$$S_R(\mathbf{v}) = \arg\left\{\max_{r\in\Re}[(x,y,z) \in \{(x,y,z): \|\mathbf{x} - (x,y,z)\| \leq r\} \Rightarrow (x,y,z) \in I_s]\right\} \tag{3}$$

where $||\mathbf{x} - \mathbf{y}||$ refers to Euclidean distance between 3-D locations $\mathbf{x}$ and $\mathbf{y}$. The $S_R(\mathbf{v})$ values correspond to the $\langle 3, 4, 5\rangle$ chamfer boundary distances computed in Stage 1.

Throughout this paper, the coordinates (x, y, z) are normalized relative to the smallest image sampling interval. For the 3-D CT images considered in this work, this smallest interval is the in-plane sampling interval $[\Delta x, \Delta y]$. Since all of 3-D CT chest images we considered were anisotropic (i.e., $\Delta x = \Delta y \neq \Delta z$), this coordinate normalization is necessary to facilitate proper processing.

Criterion (1) eliminates terminal skeletal branches that do not extend at least one voxel (Δx) beyond its parent's branch-point region; such branches are considered to be "spurs" [28]. Criterion (2) focuses on longer branches. It deletes a branch that does extend at least one radius beyond its parent's branch-point region. This eliminates a branch that is short relative to its parent's branch-point region of support, implying that the branch might appear because of a digital sampling artifact. Fig. 2(a) schematically gives examples of branches deleted by this criterion. Note that Criterion (2) catches all unwanted branches of length 2 or greater, but it does not get the distracting length-1 spurs; hence, both criteria are needed.

b) Simple centering: Skeletonization tries to produce centered branches. But, because of skeletonization's discrete nature, voxels constituting the final skeletal branches may be biased away from the ideal center by one or two voxels. Simple Centering begins to correct this improper viewing-site centering. Skeletal points are iteratively moved until they reach the locally maximal distance from the segmentation boundary.

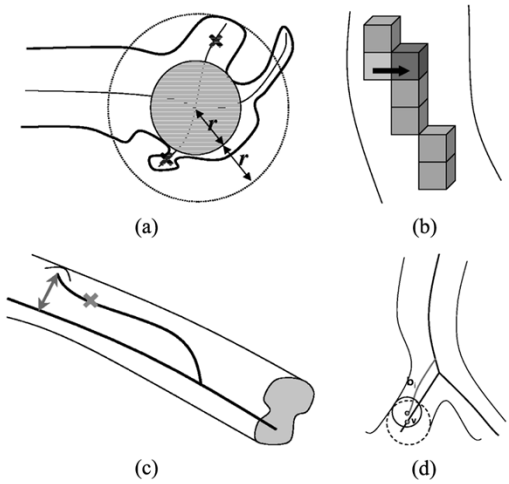

Fig. 2. Impact of Stage 2 processing. (a) Length-based elimination: the maximal sphere of radius r at a parent branch point is shown; two child branches marked by an "x" have a length $< r$ outside this maximally inscribable sphere (as indicated by radius $2r$ disk) and hence, per (2), are deleted; a third child branch is not deleted. (b) Simple centering: A viewing site (white cube) is moved (dark cube) based on maximizing its distance from the boundary. (c) Line-based elimination: Because the depicted tube has bumps on the surface, two raw branches (dark lines) arise after 3-D skeletonization. When applying line-based elimination, the double-arrow line segment connects the terminating viewing site of terminal branch to a viewing site of its parent branch; this line segment remains within the segmentation and fails the similarity measure (7); thus, the branch marked with an "x" is deleted. (d) Sphere-based elimination: the maximally inscribable sphere centered about the last viewing site of branch $\mathbf{b}_i$ and the corresponding maximally inscribable sphere centered at a viewing site $\mathbf{v}$ of another branch intersect; hence, by criterion (9), branch $\mathbf{b}_i$ is deleted.

For each viewing site $\mathbf{v}$, its 3-D location $\mathbf{x}$ is shifted in space to 3-D location $\mathbf{y}$ when

$$S_R(\mathbf{y}) > S_R(\mathbf{x}) \quad \text{and} \quad \mathbf{y} \in N_{26}(\mathbf{x}), \tag{4}$$

where $N_{26}(\mathbf{x})$ represents the 26-connected neighbors of $\mathbf{x}$ and $S_R(\cdot)$ gives the radius of a maximally inscribable sphere per (3). This operation is continued until the following condition holds:

$$\forall \mathbf{z} \in N_{26}(\mathbf{x}), \quad S_R(\mathbf{z}) \leq S_R(\mathbf{x}). \tag{5}$$

Note that viewing-site shifts have no effect on the tree's homotopy. This is because the branch structure $\mathbf{B}$ designates connections between viewing sites constituting branches, irrespective of the positions of adjacent connected viewing sites.

c) Line-based elimination: To this point, a branch will have been deleted if it is short relative to its parent's local size and volume. But it is possible to have a long terminal branch situated in nearly the same space as that occupied by a truly valid branch. Such an anomalous branch can appear, for example, if a tubular component of the tree is indented along its sides; i.e., missing voxels in I_s cut "grooves" into the tube. 3-D skeletonization can break the single branch into two branches at the beginning of such a groove. Fig. 2(c) shows an exaggerated version of this circumstance. Such a terminal branch is eliminated by this step if the branch can be reached by a sufficiently different straight-line path within the segmentation.

The detection of such a terminal branch $\mathbf{b}$ begins by computing line segments $\overline{\mathbf{v}l_{\mathbf{b}}}$ formed by connecting each viewing

site $\mathbf{v}$ of parent branch $\mathbf{b}_P$ to the final viewing site $l_{\mathbf{b}}$ (an end point) of $\mathbf{b}$. If any line segment differs too much from $\mathbf{b}$ and remains within the segmentation, then $\mathbf{b}$ is eliminated. Algorithmically, this test is defined as follows. Any terminal branch $\mathbf{b}$ that satisfies the following criterion is eliminated:

$$\exists \mathbf{v} \in \mathbf{b}_P \quad \text{such that } M_L(\mathbf{s}_{\mathbf{v}\to l_{\mathbf{b}}}, \overline{\mathbf{v}l_{\mathbf{b}}}) > D_{\text{sim}}, \quad \text{and} \quad \forall \mathbf{x} \in \overline{\mathbf{v}l_{\mathbf{b}}}, \quad I_s(\mathbf{x}) = 1 \tag{6}$$

where $\mathbf{s}_{\mathbf{v}\to l_{\mathbf{b}}}$ is the subset of viewing sites in $\mathbf{V}$ connecting $\mathbf{v}$ to $l_{\mathbf{b}}$, $\overline{\mathbf{v}l_{\mathbf{b}}}$ is the line segment connecting viewing sites $\mathbf{v}$ and $l_{\mathbf{b}}$, and $M_L(\mathbf{s}, \overline{\mathbf{yz}})$ measures the similarity between a subbranch formed by the set of n viewing sites $\mathbf{s} = \{\mathbf{s}(1), \ldots, \mathbf{s}(n)\}$ and line segment $\overline{\mathbf{yz}}$

$$M_L(\mathbf{s}, \overline{\mathbf{yz}}) = \frac{1}{n} \sum_{i=1}^{n} ||\mathbf{s}(i), \overline{\mathbf{yz}}|| \tag{7}$$

where $||\mathbf{s}(i), \overline{\mathbf{yz}}||$ is the shortest Euclidean distance between point $\mathbf{s}(i)$ and the line segment $\overline{\mathbf{yz}}$. The value D_{sim} in (6) attempts to strikes a balance between deleting and retaining such branches. Examining (6)–(7) gives

$$\sum_{i=1}^{n} ||\mathbf{s}_{\mathbf{v}\to l_{\mathbf{b}}}(i), \overline{\mathbf{v}l_{\mathbf{b}}}|| > n \cdot D_{\text{sim}} \tag{8}$$

implying that the average difference of a viewing site constituting line segment $\overline{\mathbf{v}l_{\mathbf{b}}} \subset I_s$ differs $D_{\text{sim}} \cdot \Delta x$ units (voxels) from tree subpath $\mathbf{s}_{\mathbf{v}\to l_{\mathbf{b}}}$. To have this test depict truly anomolous branches, D_{sim} should be significantly > 0. We set $D_{\text{sim}} = 4$ in our tests.

d) Sphere-based elimination: The previous simple centering step can move certain false terminal branches to the same general space as valid branches. Sphere-based elimination identifies and eliminates a terminal branch if the maximally inscribable sphere at its end point intersects a maximally inscribable sphere at any viewing site of another branch. In mathematical terms, a terminal branch $\mathbf{b}_i$ is eliminated from the tree if the following condition holds:

$$\exists \mathbf{v} \in \mathbf{V} \text{ and } \mathbf{b}_k \in \mathbf{B} \text{ such that } \mathbf{v} \in \mathbf{b}_k, \quad k \neq i, \quad \text{and} \quad (S_V(l_{\mathbf{b}_i}) \cap S_V(\mathbf{v})) \neq \emptyset \tag{9}$$

where $S_V(\mathbf{v})$ is the volume occupied by the maximally inscribable sphere centered at viewing site $\mathbf{v}$ that stays within the segmented tree I_s. Furthermore, if $\mathbf{b}_k$ is a terminal branch, then the following additional condition must hold before branch $\mathbf{b}_i$ is eliminated:

$$P(\mathbf{b}_k) \geq P(\mathbf{b}_i) \tag{10}$$

where $P(\mathbf{b})$ is the length of the longest path $\mathbf{p} \in \mathbf{P}$ containing branch $\mathbf{b}$. Fig. 2(d) illustrates a branch eliminated by this step. Note that step 3), line-based elimination, and this step do in fact detect different branches. This can be understood by considering Fig. 3(c). Two subtle details are present in this figure. First, the branch's terminal portion occurs at a "bump" on the surface. This bump supports a smaller maximally inscribable sphere for the branch's terminal portion. This sphere may not intersect with the corresponding maximally inscribable sphere of the other branch. Second, the airway's cross section is pinched, which creates a smaller maximally inscribable sphere for all points along the main branch. Thus, the requisite spheres will not intersect, leaving the branch intact after sphere-based elimination. Only line-based elimination is capable of detecting such branches.

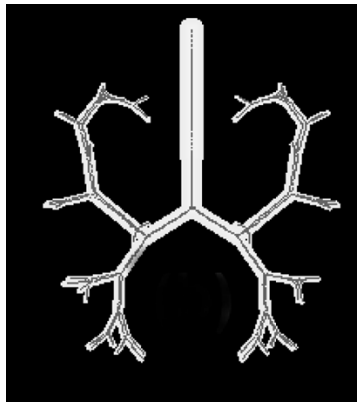

Fig. 3. Proposed method applied to a synthetic image with known branches. The image is a $300 \times 300 \times 300$ segmentation of a tree model proposed by Kitoaka *et al.* [56]. The model is comprised of branching cylinders in a mostly symmetric pattern with 125 branches and 63 paths. The diameter of each child branch ranges from 50% of its parent's to the same diameter with and average of about 80% smaller.

We now briefly justify the order of the steps above. Step 1) eliminates many useless branches, considered too short to contain significant information. This alleviates further steps from occupying processing time with such branches. One of the outcomes of Step 2) is to cause certain terminal branches that do not end within protrusions of the segmented tree to "collapse" toward the central axes of the tree. Without this step being performed first, Step 4) may not detect such spurious branches. Finally, Steps 3) and 4) are interchangeable. Note that all elements of the tree structure $\mathbf{T}$ are continually updated after each step. For example, if a parent branch has one of its child branches eliminated (assuming two child branches), then the parent and the remaining child are merged and the branch set $\mathbf{B}$ and path set $\mathbf{P}$ are updated. We again emphasize that alternate operations are conceivable for the steps above. But the primary goals of this stage—delete many of the clearly spurious branches and begin the process of better centering the axial structure—are satisfactorily accomplished by our suggested operations.

Stage 3: Tree Refinement: After stages 1 and 2, the set of paths $\mathbf{P}$ delineated by the set of viewing sites $\mathbf{V}$ still suffer from two deficiencies that render them unsuitable for 3-D navigation and quantitative analysis. First, the viewing-site locations $\mathbf{x}$ are defined with integer-valued voxel coordinates. Hence, the paths delineated by them do not accurately represent the true central axes of the tree and are not sufficiently smooth. Integer-valued viewing-site locations are especially unsatisfactory for navigation, as large angular shifts will occur from viewing site to the next [53]. Second, the viewing sites still have no viewing directions $\mathbf{d}$ associated with them. Stages 3 and 4 eradicate these deficiencies. The three operations comprising tree refinement focus on smoothing and better centering the tree branches.

a) Site elimination: Because the current viewing-site positions are defined with integer-valued coordinates, adjacent viewing sites tend to change direction abruptly. These abrupt local direction changes do not reflect the more important underlying tree structure and are in fact distracting to further analysis. What is needed is a means of capturing the general axial curvature beyond the voxel level. The approach we take uses B-spline fitting and is similar to that employed by Shani, Swift *et al.*, and Bitter *et al.* [19], [38], [54]. Applying this approach, the first step of tree refinement eliminates many unnecessary (and detrimental) viewing sites, leaving the primary skeletal structure of the tree. Subsequent tree-refinement steps smooth these data and apply B-spline analysis to generate a final set of acceptable viewing sites.

The eliminated viewing sites are chosen so that they do not alter the tree geometry, excessively shorten tree branches, or allow a subsequently fitted spline to reach outside of the segmentation I_s [Step 3) below]. Regarding this goal, most of the tree's branch points, which define the tree's branch hierarchy, and the individual branches themselves are retained. Given the branches ordered by generation and subordered by length, the following operations are applied to each branch $\mathbf{b} \in \mathbf{B}$. For each viewing site $\nu \in \mathbf{b}$, starting with $l_{\mathbf{b}}$ and considered in reverse order, eliminate any viewing site $\mathbf{v} \in \mathbf{V}$ if

$$\mathbf{v} \in S_V(\nu) \quad \text{and} \quad \mathbf{v} \neq \nu \tag{11}$$

where $S_V(\cdot)$ was defined by (9). This process preserves and favors branch points ($l_{\mathbf{b}}$ for branches $\mathbf{b} \in \mathbf{B}$). Note that it is possible, although rare for 3-D MDCT chest images, for all viewing sites to be eliminated for very short nonterminal branches. If such a branch does have all viewing sites eliminated, it is deleted from the set of branches $\mathbf{B}$ and its children are adopted by its parent by updating the branch connections in $\mathbf{P}$ and $\mathbf{B}$.

Note that the set of retained viewing sites define a "smoother" tree structure. Local ripples arising from rapid voxel-to-voxel shifts, are reduced. Only the larger, and arguably significant, branch-shape variations, as captured by the maximally inscribable spheres S_V about retained viewing sites, remain. Additionally, note that spline fitting is very sensitive to the positions of points used during fitting. When the available points are closely spaced, the fitting process in Step 3) below produces a spline reflecting the many local variations (albeit smoothly).

b) Subvoxel centering: The remaining viewing sites still have integer-valued coordinates. This step adjusts their positions to the subvoxel (noninteger) level. We employ an approach similar to that proposed by Wink *et al.* [23]. For each branch $\mathbf{b} \in \mathbf{B}$, begin with the first viewing site $\mathbf{b}(1)$ and set $l = 1$. Find the maximum value of n that satisfies the following relation:

$$M_L(\mathbf{b}_{l \to n}, \overline{\mathbf{b}(l)\mathbf{b}(n)}) < L_{\text{seg}} \tag{12}$$

where $\mathbf{b}_{l \to n}$ denotes a subset of viewing sites in $\mathbf{b}$ from $\mathbf{b}(l)$ to $\mathbf{b}(n)$ and M_L is the similarity measure (7). Operation (12) determines the longest run of viewing sites in $\mathbf{b}$ that start at $\mathbf{b}(l)$ and that fit a line segment $\overline{\mathbf{b}(l)\mathbf{b}(n)}$. The direction of this line segment is noted for all viewing sites $\mathbf{b}(l), \mathbf{b}(l+1), \ldots, \mathbf{b}(n)$. To continue, let $l = n + 1$ and repeat the process above until $l_{\mathbf{b}}$ is reached.

Next, each viewing site has its 3-D location adjusted according to the central line (CL) measure proposed by Wink *et al.* [23]. For a viewing site $\mathbf{v}$, this value measures how circular the 3-D location $\mathbf{x}$ is with respect to the cross section of I_s perpendicular to the previously computed direction. By incrementally moving the 3-D location $\mathbf{x}$, we can locally maximize the CL measure for the viewing site. This new 3-D location is assigned to $\mathbf{v}$ and better centers the viewing site within the tree. This operation is accomplished for a given viewing site $\mathbf{v}$ as follows. In the two-dimensional (2-D) cross section perpendicular to the computed direction and centered at $\mathbf{x}$, cast a series of 256 equally spaced rays emanating from $\mathbf{x}$ and reaching the boundary of the tree in I_s. Each ray $\vec{r}_{1_i}, i = 1, 2, \ldots, 128$, has a corresponding ray $\vec{r}_{2_i}$ facing in the opposite direction; i.e., $\vec{r}_{1_i}$ and $\vec{r}_{2_i}$ form a line segment. These rays are used to compute the CL measure for $\mathbf{x}$

$$\text{CL} = \frac{1}{n} \sum_{i=1}^{n} \frac{\min(|\vec{r}_{1_i}|, |\vec{r}_{2_i}|)}{\max|\vec{r}_{1_i}|, |\vec{r}_{2_i}|)}. \tag{13}$$

The CL measure is also computed for 8 evenly spaced neighbors a distance δ from $\mathbf{x}$. The point giving the maximum CL measure is used as a new intermediate value for $\mathbf{x}$. This calculation is repeated—i.e., a set of 8-neighbors a distance δ from the new $\mathbf{x}$ are found, the CL measures are computed, and the point giving the maximum CL measure is identified—until $\mathbf{x}$ gives a local maximum CL measure.

Converse to the motivation for choosing D_{sim} in (6), we use $L_{\text{seg}} = 5$ in (12). This value enables fits to reasonably long line segments ($> 2\Delta x$ units) to subsets of viewing sites, giving more gradual movements of adjacent viewing sites. For the CL test (13), we use $\delta = 0.2$. Refer to Wink *et al.* for a detailed discussion of the CL measure [23].

c) Spline fitting and smoothing: At this point, the tree $\mathbf{T}$ is similar to the discrete tree structure of Swift *et al.* [19]. The tree consists of a sparse collection of viewing-site 3-D locations $\mathbf{x}$ having floating-point values. The last step is to fit a cubic uniform (third-order) open B-spline to the 3-D locations comprising each branch and interpolate a new set of equally spaced 3-D locations along each branch fit. Viewing sites are interpolated at a resolution equal to the minimum of the x, y, and z sampling intervals (Δx for our data). This approach, applied by Swift *et al.* and Shani, provides a locally smooth set of finely sampled viewing sites for the final tree [19], [54]. Swift *et al.* give complete details on performing the B-spline fit [19].

As is well-known, a new fitted point along a B-spline curve must lie within the convex hull of the three nearest retained viewing sites; this convex hull equals the union of the set of triangles formed from each consecutive set of three viewing sites [55]. Recall from Step 1) that the viewing sites used for spline fitting, per (11), are spaced less than the locally maximally inscribable sphere inside I_s about each viewing site. While the union of these maximally inscribable spheres does not correspond precisely to the aforementioned convex hull, it typically constitutes a larger volume than the convex hull. Thus, the spline-fitted points approximately remain within I_s.

Some of the concepts employed in this stage have been used previously in some form by other researchers [19], [23], [38], [54]. Note that it is possible to perform spline fitting directly on the integer-valued viewing sites available after Stage 2. While the resulting splines would be smooth, they would have considerable distracting undulations that would not be representative of the higher-level tree structure. Step 1) of tree refinement first removes extraneous sites while retaining the important branch points. Thus, large-diameter branch regions may have few viewing sites remaining after this step, but not many are needed to compute a smooth spline through such regions. Step 2), subvoxel centering, gives a subvoxel adjustment to the remaining sites before spline fitting is performed. Again, the tree structure $\mathbf{T}$ is updated continuously during this stage.

Stage 4: Direction Setting: The 3-D locations $\mathbf{x}$ for the set of viewing sites need no further change, but the viewing directions $\mathbf{d}$ still are needed. We have devised a two-step method for producing acceptable $\mathbf{d}$.

First, $\mathbf{d}$ of each viewing site is adjusted so that it faces the final viewing site of its member branch. This is done by assigning the following viewing direction to each viewing site $\mathbf{b}(i)$ of branch $\mathbf{b} \in \mathbf{B}$

$$\mathbf{d} = \frac{\overline{\mathbf{b}(i) l_{\mathbf{B}}}}{\|\overline{\mathbf{b}(i) l_{\mathbf{B}}}\|}. \tag{14}$$

Recall that $\mathbf{d}$ is actually a quaternion. The viewing directions (14), however, are still not quite satisfactory for navigation, as sudden local twists (rolls) can occur. To prevent this circumstance, we modify the up vector ($+y$ axis in the local 3-D $x-y-z$ coordinate frame) of each viewing site's direction per the method of Paik *et al.* [27]. To do this, we leave the up vector for the first viewing site $\mathbf{b}(1)$ unchanged. Next, for $\mathbf{b}(2)$, we project $\mathbf{b}(1)$'s up vector onto the plane perpendicular to $\mathbf{b}(2) = (\mathbf{x}(2), \mathbf{d}(2))$. This projected up vector is used as the new up vector of $\mathbf{d}(2)$, giving a modified quaternion for $\mathbf{d}(2)$; note that $\mathbf{b}(2)$ will still point toward $l_{\mathbf{B}}$ after this adjustment. This process is continued for $\mathbf{b}(3), \mathbf{b}(4)$, etc., until we reach the end of the branch. (For aesthetics in viewing—in particular to prevent sudden direction changes in the vicinity of the last viewing site, our system actually reuses the same quaternion for last 5 viewing sites of a branch.)

The second step addresses interbranch continuity. Since a parent branch $\mathbf{b}_P$—constitutes a part of a path $\mathbf{p}$ through each of its child branches, a means must be used to produce smooth transitions for child viewing sites following the branch point $l_{\mathbf{b}_P}$. Without this, jumps can occur in views after a branch point. Swift *et al.* resolved this issue by interpolating a smooth path through each child branch separately, giving a highly inefficient data structure that would repeat viewing sites and branches for multiple paths [19]. We resolve these discontinuities, while keeping a single tree structure, by using spherical linear interpolation [42], [43]. The viewing directions $\mathbf{d}(i)$ for the first 9 viewing sites of a child branch $\mathbf{b}$ are modified as follows:

$$\bar{\mathbf{d}}(i) = \frac{\mathbf{d}(i) \sin\left(\frac{i\theta}{9}\right) + \mathbf{d}_{l_{\mathbf{b}_P}} \sin\left(\theta - \frac{i\theta}{9}\right)}{\sin(\theta)}, \quad i = 1, 2, \ldots, 9 \tag{15}$$

where $\bar{\mathbf{d}}(i)$ is the final viewing direction for $\mathbf{b}(i)$ (child branch $\mathbf{b}$'s ith viewing site), $\mathbf{d}(i)$ is the previous viewing direction for $\mathbf{b}(i)$, $\mathbf{d}_{l_{\mathbf{b}_P}}$ is the viewing direction for the branch point spawning the child branch $\mathbf{b}$, and

$$\theta = \cos^{-1}\left(\mathbf{d}(i) \cdot \mathbf{d}_{l_{\mathbf{b}_P}}\right)$$

is the angle between the directions of $\mathbf{b}(i)$ and $l_{\mathbf{b}_P}$. The weights in (15) gradually diminish the branch point's influence on the final direction calculation. For example, $i = 0$ defaults to $\mathbf{d}_{l_{\mathbf{b}_P}}$, while $i = 9$ gives $\mathbf{d}(9)$ (no change). The choice to modify the first 9 viewing-site directions can, of course, be changed and is motivated by aesthetics in viewing. Our proposal assumes a 90° worst-case direction change from branch point $l_{\mathbf{b}_P}$ to child branch $\mathbf{b}$'s first viewing site $\mathbf{b}(1)$, implying a gradual 10° maximum direction change for the initial set of viewing sites. Wink *et al.* also noted the potential for abrupt direction changes in branches and used an approach similar to (15) to ameliorate this difficulty [23].

C. Implementation Issues

The final output of the method is the tree data structure $\mathbf{T} = \{\mathbf{V}, \mathbf{B}, \mathbf{P}\}$. The viewing sites $\mathbf{v} = (\mathbf{x}, \mathbf{d})$ constituting $\mathbf{V}$ have floating-point 3-D positions $\mathbf{x}$ and viewing directions $\mathbf{d}$. The set $\mathbf{B}$ consists of branches deemed significant in the presegmented input image I_s. These branches in turn constitute the paths $\mathbf{p} \in \mathbf{P}$, which all begin with root branch $\mathbf{b}_1$ and terminate with a branch having an end point. The final paths are defined to the subvoxel level and offer smooth viewing direction transitions.

The complete method integrates a number of ideas proposed by previous researchers working in the fields of skeletonization, path planning, branch delineation, and graphical navigation [19], [23], [27], [42]–[46], [54] in addition to several new concepts. The Stage-1 3-D skeletonization method is tailored to tree-like structures and is a hybrid combination of previously proposed methods. The Stage-2 operations have not been proposed previously to the best of our knowledge, but are related to the simple skeletal pruning ideas used by others for deleting short branches (e.g., [32]). A novel aspect of the Stage-2 operations is that they eliminate a branch based on its actual shape and size (as represented in I_s), as opposed to just its skeletal length. Stages 3 and 4 combines ideas from a few previous methods, but the concept for generating smooth viewing directions across branches, resulting in final smooth paths well-suited for visual navigation inside the human airway tree, is new.

Our computer implementation uses several discrete approximations. For example, line-based elimination uses line segments in (6) that are sampled at nearest integer-coordinate points along their length. Similar digital approximations are used for the maximally inscribable spheres in (9) for sphere-based elimination and (11) for site elimination. These approximations in principle can affect the accuracy of these steps to roughly ± 1 unit. But given the high resolution of our MDCT data (Section III) and the subvoxel corrective aspects of tree refinement, we have found no adverse influence from these small approximations.

The method requires no difficult parameter choices, but values for the preselected root site, $D_{\text{sim}}, L_{\text{seg}}$, and δ warrant comment. First, as discussed in Section III, the preselected root site can be chosen easily and over a wide range near the proximal end of the trachea. For line-based elimination [stage 2, Step 3)], the discussion for (8) gives rationale for choosing D_{sim}. To add further insight, this value relates directly to the diameter of branches in the segmented tree I_s. Line-based elimination is intended for deleting false branches that spawn off of bifurcations near large branches. If D_{sim} is larger than the diameter of I_s's largest branch, then no branch can be eliminated by test (6). The choice of L_{seg} and δ in subvoxel centering [stage 3, Step 2)] do not affect the tree's final geometry (i.e., the number of tree branches), but instead influence the curvature and direction of the final branches. Hence, the impact of L_{seg} and δ is minor. Following the discussion in stage 3, Step 2), we see little reason to increase L_{seg} beyond 5. See Wink *et al.* for a discussion of the CL measure (13) which employs δ. Our parameter values were found empirically by studying visual results generated from 3-D CT human images using our VB system.

In principle, the method attempts to define branches for significant tubular (branch-like) components in I_s. While the discrete approximations make it difficult to rigorously prove properties of final tree branches, it can be stated that only branches originating in the 3-D skeleton of I_s can appear in the final tree $\mathbf{T}$. Further, each terminal branch must extend a minimum length beyond its parent's end point, per (1)–(2). In practice, our goal has been to devise a method that extracts "a sufficient number" of airway paths to enable MDCT assessment and follow-on guided bronchoscopy to sites reachable by modern bronchoscopes (see Section IV discussion).

III. Results

Results are presented focusing on the performance of the proposed method and on applications to VB-based assessment of lung cancer.

A. Method Performance

Fig. 3 gives an initial test of the method for a synthetic 3-D airway-tree image with a known branching structure, proposed by Kitaoka *et al.* [56]. As the synthetic model is very simple, with no degradations, the proposed method agreed completely with the predefined known branches. Branch agreement was based on how well branch points and end points of corresponding branches matched. Branch points had to be at the same hierarchical level of the tree to agree, while the difference between 3-D locations of corresponding branch points and end points had to be less than or equal to six voxels (this was the value needed to enable complete agreement).

We next ran a series of tests on real human images. Twelve 3-D human CT chest images were used to compare the proposed method to the previously developed branch-following method of Swift *et al.* [19]. These images were acquired from either a Philips MX8000 MDCT scanner, Imatron electron-beam CT (EBCT) scanner, or Toshiba Aquilion MDCT scanner. The subjects included airway, lung nodule, and mediastinal lymph-node cases, and all were studied under a protocol approved by the University of Iowa IRB. All scans required one 20-s breath hold by the subject. All slices consisted of 512×512 voxels in the transverse plane, but the number of slices for the 12 images varied from 100 to 597. Eight images were from seven subjects scanned in the MX8000. For one MX8000 subject, we included two images, where the ventilation level [functional residual capacity (frc) or total lung capacity (tlc)] was varied. The anisotropic voxels in these images had in-plane resolutions $\Delta x = \Delta y$ ranging from 0.57 mm to 0.59 mm, and Δz resolution (slice-to-slice spacing) 0.60 mm. Three images were from three different subjects scanned on the Imatron EBCT scanner, with $\Delta x = \Delta y = 0.586$ mm or 0.684 mm and Δz resolutions of 1.50 mm or 3.0 mm. The remaining data set was generated on the Toshiba scanner, with $\Delta x = \Delta y = 0.6$ mm and $\Delta z = 3.0$ mm. We point out that these 12 test images contain over 1000 branches, giving a more than sufficient variety of test situations. A dual-CPU Dell workstation, using 933 MHz Intel Xeon Pentium-III processors, 2 GB of RAM, and Windows 2000, was used for all tests.

TABLE I
Tree Analysis Results for the Previously Developed Branch-Following Method of Swift *et al.* [19] Versus the Proposed Method. The Results Were Taken Over Twelve 3-D Human CT Scans

Item	Swift		Proposed	
	μ	σ	μ	σ
Branches	52.0	34.7	90.3	60.9
Paths	29.2	19.8	46.4	31.3
Maximum Generation	7.0	2.4	9.7	2.8
Time (sec)	70		130	

"Branches" denotes the number of final branches produced, "paths" signifies the number of paths produced, and "maximum generation" is the highest-generation output branch (generation 1 denotes the root branch). For these three measures, both the mean μ and standard deviation σ are given. "Time" denotes average computation time.

Root sites were preselected by a human operator, who examined transverse and coronal CT sections in our VB system [6], [19]. We point out that these root sites, positioned near the proximal end of the trachea, are very easy to find. Considerable flexibility exists in picking a root site, since the trachea is generally the longest branch of the airway tree. On tests with four MDCT human images, we varied the root site over a range of 5–20 slices and a 15×15 or a 20×20 square of voxels in the transverse plane (this is comparable to the typical cross-sectional area of the trachea which consists of about 400–600 voxels on a 2-D slice or 150–250 mm^2). We found no changes in the resulting branch geometries and only minor local changes in proximal ends of the root (tracheal) branches $\mathbf{b}_1$.

Tables I–III and Fig. 4 present comparison results for the proposed method and the Swift *et al.* branch-following method. As part of this table, we present results on branches deemed to be correct or in error. An expert observer used several visualization tools in our interactive VB system to judge the correctness of the extracted branches. The visualization tools used were as follows: (a) transverse slices; (b) local cross sections orthogonal to each viewing site along a branch; (c) local cross sections parallel to each viewing site along a branch; and (d) coronal front-to-back depth-weighted maximum thin slab

TABLE II
CASE-BY-CASE TREE ANALYSIS RESULTS FOR THE SWIFT *et al.* BRANCH-FOLLOWING METHOD AND PROPOSED METHOD. SAME TWELVE CASES AS IN TABLE I USED

Image	Swift				Proposed		
	gen.	branches	errors	fail?	gen.	branches	errors
d	7	22	2		7	23	0
sub7	6	33	6		6	23	0
v	9	50	3	yes	10	62	1
h001	8	83	13	yes	15	198	20
h002	7	121	23	yes	12	176	12
h004	9	63	13		9	57	1
h005	9	97	24		10	96	11
h008	9	53	7	yes	12	147	0
h015	4	13	0	yes	9	49	2
h018frc	8	41	10	yes	11	78	2
h018tlc	7	44	9	yes	10	141	20
h023	1	3	0	yes	5	34	0

For each image (identified by a coded name), the number of branch generations (gen.), the total number of branches (branches) computed, and the erroneous branches (errors) computed by each method is listed. For the swift method, an additional column indicates whether the method failed to produce an acceptable result; Table III gives the nature of these errors and Fig. 4 shows examples of two failures.

TABLE III
FOR EACH FAILED IMAGE OF TABLE II, THE NATURE OF THE FAILURE OF THE SWIFT METHOD IS GIVEN

Image	Nature of Failure
v	paths only found in left lung
h001	several gens. missing; few paths in left upper lobe or right upper lobe
h002	several generations missing
h008	several gens. missing; no paths in left upper lobe
h015	very few branches found
h018frc	paths only in left lung
h018tlc	several gens. missing; no paths in left upper lobe
h023	a near total failure; 2 branches barely advance beyond main carina

views $(\text{focus} = 20, \text{vision} = 30, \text{window max} = 400)$, which clearly shows the contours of airways as they are traversed along a branch [57]. The cross section views were windowed in the $[-800\ 240]$ range to sharply defined airway walls for small airways. The expert ran the system in "movie mode," which enabled observation of a branch in all visualization tools simultaneously. It was apparent that all branches >2 generations from terminating branches were correct. So, the expert observer focused on branches situated in the peripheral 2–3 generations for each case; this still required the observer to interrogate on the order of 60% of the branches. As the branches in question were typically in the distant periphery, they were generally very short with little spatial support. Hence, judgments on these branches were often difficult. The structure of the tree also helped in identifying possible erroneous branches. Many branches deemed to be erroneous arose from implausible trifurcations or from bifurcations that arose in rapid succession (i.e., a false bifurcation may have occured). Also, branch following appeared to produce branches that "circled around" an open space without regard for whether the space had already been covered earlier.

Per Tables I–II, the proposed method generally produces many more correct branches (1015 total over all images) than branch following (513 total), while giving fewer erroneous branches ($69/1084 = 6.4\%$ versus $110/623 = 17.7\%$). Branch following did produce more correct branches for one thick-slice Toshiba case (sub7), but these branches were very small and the dataset gave little spatial support for many branches. (We must emphasize that nearly all of the so-called erroneous branches found for the various images were very small and in the far distant periphery. Hence, their significance is questionable.) As Table II shows, branch following gave significant failures for 8 of 12 cases, while the proposed method never fails. Two of these failures are shown in Fig. 4. Branch following is unduly sensitive to rapid changes in the airway structure, causing branch following to halt early in defining the tree. Unfortunately, rapid changes in airway structure often correspond to the presence of a pathology, such as a stenosis or impinging tumor, exactly the structures the physician wishes to examine. For case h023, branch following was barely able to produce a tree at all (only three branches). Further, the proposed method generally captured over two more generations of branches on average than branch following (mean values of 9.7 versus 7.0).

The generated trees agreed on the number of extracted branches up to generation 3.2 on average, where the root branch was counted as generation 1. Branch agreement was based on the criteria used for the Kitaoka phantom result.

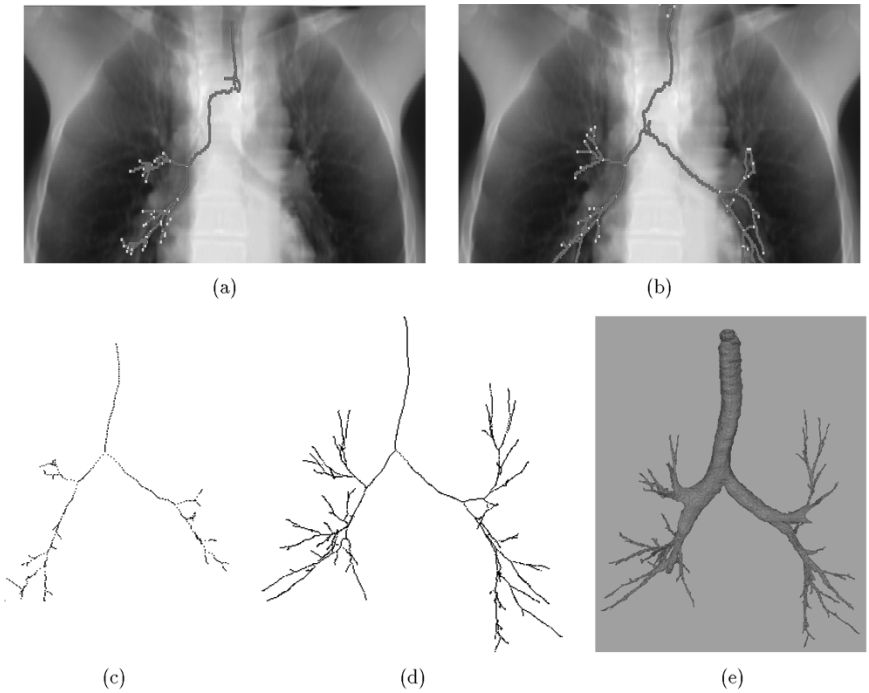

Fig. 4. Pictorial comparison of Swift *et al.* and the proposed method. (a)–(b) Coronal depth-weighted coronal projection images for image v (the lines are the extracted 3-D paths projected onto the coronal plane). The Swift method gives no information in the left lung. (c), (d) Coronal projections of the paths obtained for the case h008 with (c) the branch-following method of Swift *et al.* and (d) the proposed method. (e) A 3-D surface rendering of the input segmented airway tree I_s. The proposed method recovers more peripheral branches than branch following (see Table II).

TABLE IV
PERFORMANCE BREAKDOWN OF PROPOSED METHOD. THE NUMBER OF BRANCHES, % OF BRANCHES DELETED, COMPUTATION TIME (SECONDS), AND % OF TOTAL COMPUTATION TIME ARE GIVEN FOR EACH STAGE. A SEPARATE BREAK-OUT IS ALSO GIVEN FOR THE BRANCH-ELIMINATION STEPS OF STAGE 2

Stage/Step	No. of Branches Deleted	% of Branches Deleted	Computation Time (sec)	% of Computation Time
Stage 1: Skeletonization	205*	n/a	133	84.8
Stage 2: False Branch Elimination	117.2	56.9	10.7	6.8
Step 1: Length-based	113	54.9		
Step 3: Line-based	1.3	0.6		
Step 4: Sphere-based	2.9	1.4		
Stage 3: Tree Refinement	2.3	1.1	10.7	6.8
Stage 4: Direction Setting	—	—	2.43	1.6
total branches deleted	118.7	58.0	n/a	n/a

Note that stage 4 and step 2 of stage 2 do not delete any branches. The 205* entry for skeletonization gives the starting number of branches before any deletion occurs. Results are based on an average over seven 3-D CT images.

Since branch following tended to produce shorter terminal branches, we also allowed for a six-voxel tolerance in position difference for matching end points. Despite this tolerance, other corresponding branches, ruled to be different, actually appear visually similar. Note that the matching of anatomical trees generated from image processing is an open research problem, and work is in progress [50], [52]. Hence, our comments on tree matching and on the numbers of significant branches are not rigorous. As pointed out in Section I, airway trees are very complex and essentially impossible to define manually. Hence, gold-standard data is not available. Yet, detailed visual inspection, as shown in Fig. 4, supports our conclusion that the proposed method produces more significant branches than branch following.

Regarding execution time, the proposed method ran in 130 s on average, including prior segmentation times to generate I_s, while branch following ran in 70 s on average, including multiple executions for parameter adjustments. A substantial drawback of the branch-following method, however, not reflected in mere computer execution time is that the human operator must run the method two or three times typically to test parameter adjustments and must then examine the intermediate results between runs. This factor makes branch following much more time consuming and subject to human operator experience.

Table IV gives a performance breakdown for the proposed method, averaged over seven 3-D images. 3-D Skeletonization accounts for 84.8% of the computation, but this step processes all data within the segmentation I_s. The subsequent three stages only examine the small amount of data captured in the tree representation $\mathbf{T}$. Length-based elimination deletes the large majority of distracting branches, yet the remaining steps do delete significant distracting branches, particularly in cases with complex pathologies (e.g., Fig. 5).

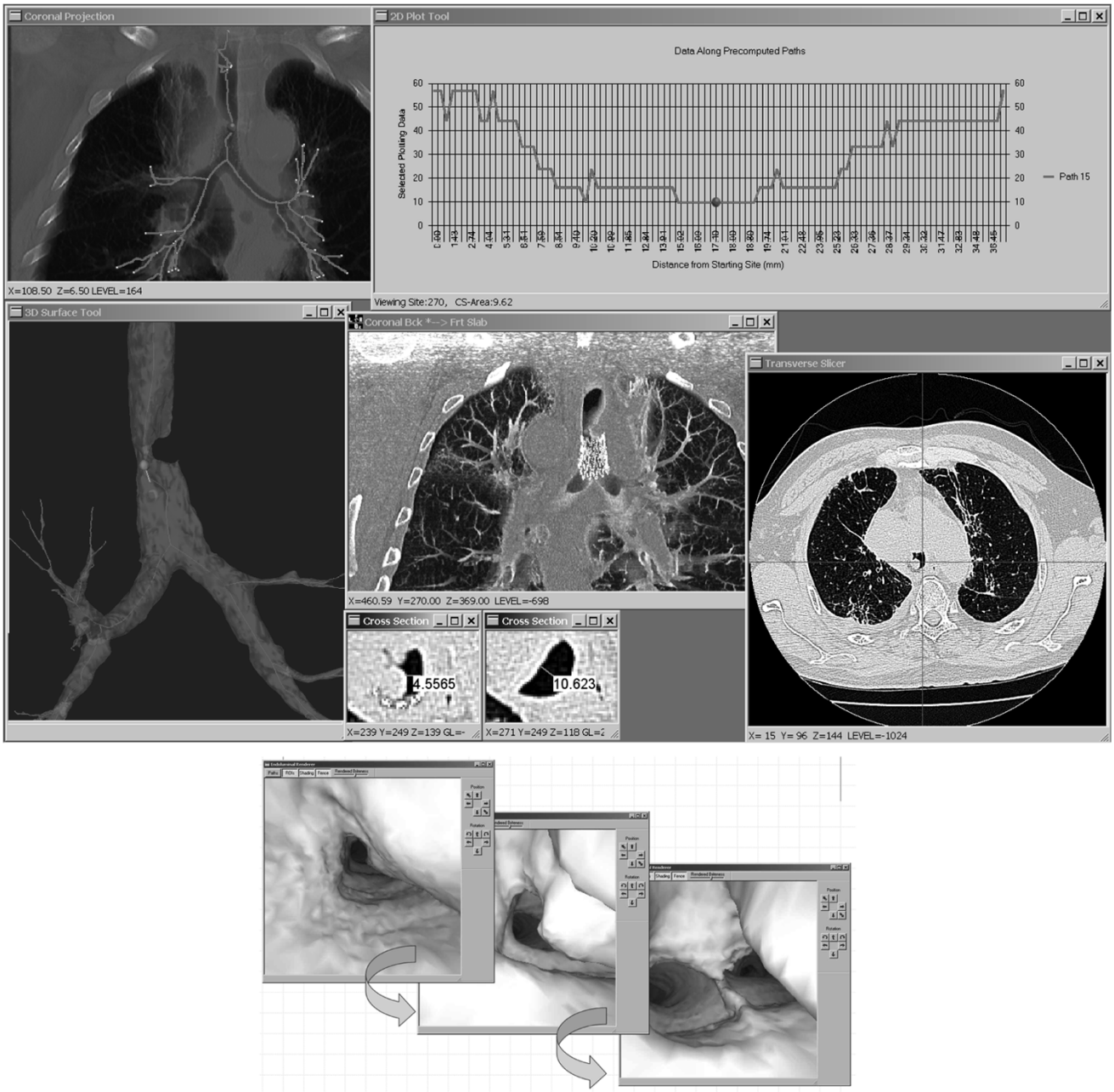

Fig. 5. Airway-obstruction case. (Top view) Coronal Projection Tool shows a weighted-sum coronal projection of the 3-D CT image ($240 \leq y \leq 295$ used in projection calculation), with overlaid quantitative paths (red lines) and branch points (green squares). The blue dot lies within the most obstructed portion of the trachea and signifies the viewing site focused on by all other tools. 3-D Surface Tool zooms in on the pertinent obstructed portion of the rendered segmented airway tree, with quantitative paths again overlaid; the yellow sphere is the viewing site of interest. 2-D Plot Tool shows a plot of airway cross-sectional airway versus distance along the airway. The data is plotted for a subset of viewing sites situated about the obstructed airway (path 15, sites 150–248). The blue plot site is the viewing site of interest; the drop in cross-sectional area is apparent. $\mathrm{Coronal\ Bck}^{*} - > \mathrm{Frt\ Slab}$ Tool depicts a depth-weighted maximum thin slab of data in the coronal direction, situated about the viewing site (the red dot) (back-to-front view, $\mathrm{focus} = 20, \mathrm{vision} = 30$, data processing and viewing windows use range $[-1024, 1000]$ [57]). Previously inserted wire-mesh stent is clear in this view. Transverse Slicer shows a slice at selected viewing site, with cross-hairs signifying location ($\mathrm{viewing\ window} = [-1000, 200]$). Impinging cancer is clear in this view. Cross Section tool shows a local cross section orthogonal to the viewing site; width of airway is 4.5565 mm at this site, as shown (3.0 × zoom, viewing window: $[-1000, 200]$). A second cross section at a different viewing site above the obstruction shows a normal-looking cross section, with a measured $\mathrm{width} = 10.623$ mm. (Bottom view) Sequence of three endoluminal airway renderings along the obstructed airway, following path highlighted above. (Case parameters: image ge_flip, $512 \times 512 \times 373, \Delta x = \Delta y = 0.647, \Delta z = 0.5, \mathrm{root\ site} = (244, 217, 0)$, segmentation RG, $\mathrm{e} = 50\,000$, no filter, followed by simple morphological reconstruction).

B. Applications to Human VB-Based Lung-Cancer Assessment

As mentioned in Section I, we have devised an interactive computer-based system for VB assessment of lung-cancer patients. More details on the system appear in [6] and [7]. The proposed path-planning method plays a vital role in this system. Below, we present two cases.

Case 1) A 57-year-old male lung-cancer patient, previously fitted with a nitinol stent, underwent a Toshiba Aquilion 3-D MDCT scan. A technician then performed 3-D airway-tree segmentation [20], root-site definition, and path analysis; these procedures took roughly 20 min. A physician then inspected the case and defined the site of interest, situated

Fig. 6. Virtual bronchoscopic examination at a site of an encroaching stent [19]. Composite VB-guidance system view depicts the 3-D CT scan registered to the bronchoscopic video near the site of the stent. (Top View) System's Video Match Tool. The tool accepts the bronchoscopic video and matches it to the polygonal surface data obtained from the original EBCT data. The Top-left view is the free-running bronchoscopic video (distortion corrected) and the Top-right view depicts the matched endoluminal airway surface view; the red line is the precomputed path being followed. The CT scan had been done several months earlier after initial stent insertion. The virtual endoluminal view shows a protruding portion of the stent before tissue grew over it. (Bottom View) The matched CT-video location is also displayed in the other two views. The Coronal Projection Tool shows weighted-sum coronal projection of the CT data (slice data in the range $200 \leq y \leq 300$ used); red lines represent the precomputed paths and the blue dot gives the current examination site. The 3-D Surface Tool depicts a rendering of the segmented airway tree, navigation paths, and current site; the current site and viewing direction are represented as a ball and needle. An airway obstruction beyond the right main bronchus results in few airways paths in the right lung. (Case parameters: image d001010, $512 \times 512 \times 123$, Imatron EBCT scan, $\Delta x = \Delta y = 0.586$ mm, $\Delta z = 1.5$ mm, root site $= (250, 257, 5)$, segmentation RG, $\mathrm{e} = 50\,000$, no filter).

near the impinging cancer. The technician then selected a path that "flies by" this site for use during follow-on quantitative analysis and guidance. This path is easily selected by pointing to the desired location on the Coronal Projection Tool or 3-D Surface Tool (see Fig. 5). These procedures required roughly 15 min. (Note that branch following could not generate a path that passed through the pathology.)

Fig. 5 gives a composite after these steps. Since the 3-D airway-surface rendering and coronal projection plainly show the primary lung cancer in the distal trachea growing above the stent, it was straightforward to select a path for airway analysis. In general, path selection is done very easily, as the preselected sites are usually near one of the visible airways. Also, because of the diameters of current bronchoscopes, no branches beyond generation 7 generally are necessary. The cross-sectional area plot and other views clearly depict other manifestations of the lingering obstruction. Post Nd:YAG laser surgery later followed to mitigate the obstruction.

Case 2) A 43-year-old female patient presented bleeding in the airways, as a result of a stent previously inserted into the right main bronchus. Using an Imatron EBCT scan collected earlier, 3-D airway-tree segmentation, root-site selection, and path analysis was done. These procedures again took approximately 20 min. The computed data were then interrogated in our VB guidance system to select a path passing through the stent region.

The computer system was brought into the bronchoscopy suite and interfaced to the bronchoscope. This interfacing required roughly 15 min, and the bronchoscope had previ-

ously been calibrated for distortion correction [58]. After this preparation, with the aid of the technician, the physician performed a virtually guided bronchoscopy to the region of the stent. Nd:YAG laser surgery then followed to trim the impinging portion of the stent. Fig. 6 gives a composite view in the vicinity of the stent. These results draw upon a technique based on normalized mutual information for registering the "virtual world" of the CT-based rendered endoluminal airway views to the "real world" of the bronchoscopic video. References [7], [59] give details on this procedure. To the best of our knowledge, this case is the first demonstration of direct image guidance of live bronchoscopy.

IV. Discussion

To date, we have successfully used the proposed path-planning method in tandem with our image-guided bronchoscopy system on over 90 human lung-cancer patients. Studies with these patients have involved mediastinal lymph-node biopsy, peripheral-nodule analysis, and airway-obstruction analysis [60]–[64]. Reference [7] gives a description of the complete system and provides examples of virtually guided mediastinal lymph-node biopsy. We point out that 3–4 defined airway generations tend to be sufficient for planning and guiding procedures for airway obstructions (e.g., stent insertion and Nd:YAG laser surgery) and most mediastinal lymph-node biopsies. Bronchoscope technology, which currently employs 6 mm diameter devices, defines this limitation. Physicians, however, have observed on the order of 8 to 10 airway generations using new ultrathin bronchoscopes ($\text{diameter} = 2.6$ mm) [65]. For current MDCT scanning technology, our path-planning method visually appears to produce on the order of 10 generations of valid airway branches.

While our proposed method generates a large number of apparently correct branches, we caution that "false branches" may still exist, and no one, to the best of our knowledge, has defined a complete anatomically correct description of a 3-D tree captured by a 3-D CT scan. Image data degraded by excessive image reconstruction artifacts (e.g., from so-called "sharp" reconstruction kernels) can produce false branches. Application-dependent model-based criteria [56] or more sophistated graphical editing [51], [52] may be necessary to produce a definitively correct and complete tree. The problem of accurate hierarchical tree definition is the topic of ongoing research [50], [52] and has not impeded our efforts for image-guided bronchoscopy, which does not require a complete tree.

The proposed method has proven to be practical in the clinical arena of human lung-cancer patient management. The method typically requires 3 min to run on a medium-range PC, with the longest observed time at 5.3 min. We point out that these times are for very large 3-D MDCT chest scans (200–300 MBytes of image data per typical scan). When the path-planning method is coupled with the tasks of performing the prior airway-tree segmentation and root-site selection, the total time for interaction and preparation is comfortably under 20 min. The only human interactions required are the straightforward selection of the airway tree's root site and physically running the programs. All tasks can be accomplished by a trained technician. While our primary interest has been to apply the method to the planning and guidance of bronchoscopy, we have also applied the method successfully to a large variety of 3-D images, including 3-D CT airway scans of phantoms, animals, and humans, in addition to 3-D micro-CT vascular-tree images [66], [52].

Finally, we would like to offer some historic comments on the field of virtual bronchoscopy. All major CT scanner manufacturers have offered some form of endoluminal airway viewing on their scanner workstaions since 1996–1997. This simple viewing operation has essentially defined what VB is. Many small pilot studies have been done that address the potential of VB for CT image assessment, but none have definitively confirmed VB's lasting clinical value. Yet, we believe virtual bronchoscopy (probably the wrong term to use) needs to go well beyond simple endoluminal airway viewing to become a clinically accepted tool. It has been our goal to wed this basic methodology with many other methodologies in image processing, computer graphics, and clinical devices to produce a system for the planning and true guidance of bronchoscopy.

Acknowledgment

The authors would like to thank: Dr. R. Swift for the code used to implement the spline fitting portion of the method; A. Sherbondy, A. Austin, J. Turlington, and D. Zhang for their contributions to the VB system; and A. Delsing, J. Cook-Granroth, and J. Sieren for their technical assistance with the human 3-D CT cases.

References

[1] W. Kalender, *Computed Tomography: Fundamentals, System Technology, Image Quality, Applications*. Munich, Germany: Publicis MCD Verlag, 2000.

[2] E. A. Kazerooni, "High resolution CT of the lungs," *Amer. J. Roentgenol.*, no. 3, pp. 501–519, Sept. 2001.

[3] I. Bricault, G. Ferretti, and P. Cinquin, "Registration of real and CT-derived virtual bronchoscopic images to assist transbronchial biopsy," *IEEE Trans. Med. Imag.*, vol. 17, pp. 703–714, Oct. 1998.

[4] H. P. McAdams, P. C. Goodman, and P. Kussin, "Virtual bronchoscopy for directing transbronchial needle aspiration of hilar and mediastinal lymph nodes: A pilot study," *Amer. J. Roentgenol.*, vol. 170, pp. 1361–1364, May 1998.

[5] K. Hopper, T. Lucas, K. Gleeson, J. Stauffer, R. Bascom, D. Mauger, and R. Mahraj, "Transbronchial biopsy with virtual CT bronchoscopy and nodal highlighting," *Radiology*, vol. 221, no. 2, pp. 531–536, Nov. 2001.

[6] J. P. Helferty, A. J. Sherbondy, A. P. Kiraly, J. Z. Turlington, E. A. Hoffman, G. McLennan, and W. E. Higgins, "Image-guided endoscopy system for lung cancer assessment," in *Proc. IEEE Int. Conf. Image Processing 2001*, Oct. 7–10, 2001, pp. 307–310.

[7] J. P. Helferty, A. Kiraly, A. Sherbondy, E. Hoffman, G. McLennan, and W. E. Higgins, "System for the virtual guidance of bronchoscopy," *IEEE Trans. Med. Imag.*, 2004, submitted for publication.

[8] W. E. Lorensen, F. A. Jolesz, and R. Kikinis, "The exploration of cross-sectional data with a virtual endoscope," *Interactive Technol. New Health Paradigm*, pp. 221–230, Jan. 1995.

[9] G. D. Rubin, C. F. Beaulieu, V. Argiro, H. Ringl, A. M. Norbash, J. F. Feller, M. D. Dake, R. B. Jeffrey, and S. Napel, "Perspective volume rendering of CT and MR images: Applications for endoscopic imaging," *Radiology*, vol. 199, no. 2, pp. 321–330, May 1996.

[10] D. J. Vining, K. Liu, R. H. Choplin, and E. F. Haponik, "Virtual bronchoscopy: Relationships of virtual reality endobronchial simulations to actual bronchoscopic findings," *Chest*, vol. 109, no. 2, pp. 549–553, Feb. 1996.

[11] R. M. Summers, "Navigational aids for real-time virtual bronchoscopy," *Amer. J. Roentgenol.*, vol. 168, no. 5, pp. 1165–1170, May 1997.

[12] W. E. Higgins, K. Ramaswamy, R. Swift, G. McLennan, and E. A. Hoffman, "Virtual bronchoscopy for 3-D pulmonary image assessment: State of the art and future needs," *Radiographics*, vol. 18, no. 3, pp. 761–778, May–June 1998.

[13] H. P. McAdams, S. M. Palmer, J. J. Erasmus, E. F. Patz, J. E. Connolly, P. C. Goodman, D. M. Delong, and V. F. Tapson, "Bronchial anastomotic complications in lung transplant recipients: Virtual bronchoscopy for noninvasive assessment," *Radiology*, vol. 209, no. 3, pp. 689–695, Dec. 1998.

[14] R. M. Summers *et al.*, "Polypoid lesions of airways: Early experience with computer-assisted detection by using virtual bronchoscopy and surface curvature," *Radiology*, vol. 208, no. 2, pp. 331–337, Aug. 1998.

[15] E. F. Haponik, S. L. Aquino, and D. J. Vining, "Virtual bronchoscopy," *Clinics Chest Med.*, vol. 20, no. 1, pp. 201–217, Mar. 1999.

[16] S. L. Aquino and D. J. Vining, "Virtual bronchoscopy," *Clinics Chest Med.*, vol. 20, no. 4, pp. 725–730, Dec. 1999.

[17] K. Mori, J. Hasegawa, Y. Suenaga, and J. Toriwaki, "Automated anatomical labeling of the bronchial branch and its application to the virtual bronchoscopy system," *IEEE Trans. Med. Imag.*, vol. 19, pp. 103–114, Feb. 2000.

[18] G. Ferretti, F. Thony, J. Bosson, C. Pison, F. Arbib, and M. Coulomb, "Benign abnormalities and carcinoid tumors of the central airways: Diagnostic impact of CT bronchography," *AJR*, vol. 174, pp. 1307–1313, May 2000.

[19] R. D. Swift, A. P. Kiraly, A. J. Sherbondy, A. L. Austin, E. A. Hoffman, G. McLennan, and W. E. Higgins, "Automatic axes-generation for virtual bronchoscopic assessment of major airway obstructions," *Computerized Med. Imag. Graphics*, vol. 26, no. 2, pp. 103–118, Mar.–Apr. 2002.

[20] A. P. Kiraly, E. A. Hoffman, G. McLennan, W. E. Higgins, and J. M. Reinhardt, "3-D human airway segmentation methods for virtual bronchoscopy," *Academic Radiol.*, vol. 9, no. 10, pp. 1153–1168, Oct. 2002.

[21] R. M. Summers, N. R. Aggarwal, M. C. Sneller, M. J. Cowan, B. J. Wood, C. A. Langford, and J. H. Shelhamer, "CT virtual bronchoscopy of the central airways in patients with Wegener's granulomatosis," *Chest*, vol. 121, no. 1, pp. 242–250, Jan. 2002.

[22] R. Azuma, "A survey of augmented reality," *Presence: Teleoperators Virtual Environ.*, vol. 6, no. 4, pp. 355–385, Aug. 1997.

[23] O. Wink, W. J. Niessen, and M. A. Viergever, "Fast delineation and visualization of vessels in 3-D angiographic images," *IEEE Trans. Med. Imag.*, vol. 19, pp. 337–346, Apr. 2000.

[24] K. Krissian, G. Malandain, and N. Ayache, "Model-based detection of tubular structures in 3-D images," *Comput. Vis. Image Understanding*, vol. 80, no. 2, pp. 130–171, Nov. 2000.

[25] C. C. Hanger, S. T. Haworth, R. A. Molthen, and C. A. Dawson, "Semi-automated skeletonization of the pulmonary arterial tree in micro-CT images," *SPIE Med. Imaging 2001: Physiol. Funct. From Multidim. Images*, vol. 4321, pp. 510–516, Feb. 18–20, 2001.

[26] S. R. Aylward and E. Bullitt, "Initialization, noise, singularities, and scale in height ridge transversal for tubular object centerline extraction," *IEEE Trans. Med. Img.*, vol. 21, pp. 61–75, Feb. 2002.

[27] D. S. Paik, C. F. Beaulieu, R. B. Jeffrey, G. D. Rubin, and S. Napel, "Automated flight path planning for virtual endoscopy," *Med. Phys.*, vol. 25, no. 5, pp. 629–637, May 1998.

[28] V. Sauret, K. A. Goatman, J. S. Fleming, and A. G. Bailey, "Semi-automated tabulation of the 3-D topology and morphology of branching networks using CT: Application to the airway tree," *Phys. Med. Biol.*, vol. 44, pp. 1625–1638, 1999.

[29] K. Mori, Y. Suenaga, J. Toriwaki, J. Hasegawa, K. Katada, H. Takabatake, and H. Natori, "A method for tracking camera motion of real endoscope by using virtual endoscopy system," *SPIE Med. Imag. 2000: Physiol. Function from Multidimensional Images*, vol. 3978, pp. 122–133, Feb. 12–17, 2000.

[30] D. Selle, P. Preim, A. Schenk, and H. O. Peitgen, "Analysis of vasculature for liver surgical planning," *IEEE Trans. Med. Img.*, vol. 21, pp. 1344–1357, Nov. 2002.

[31] E. Sorantin, C. Halmai, B. Erdöhelyi, K. Palágyi, L. G. Nyúl, K. Ollé, B. Geiger, F. Lindbichler, G. Friedrich, and K. Kiesler, "Spiral-CT-based assessment of tracheal stenoses using 3-D skeletonization," *IEEE Trans. Med. Imag.*, vol. 21, pp. 263–273, Mar. 2002.

[32] S. Wood, E. Zerhouni, J. Hoford, E. Hoffman, and W. Mitzner, "Measurement of three-dimensional lung tree structures by using computed tomography," *J. Appl. Physiol.*, vol. 79, pp. 1687–1697, 1995.

[33] C. Pisupati, L. Wolff, W. Mitzner, and E. Zerhouni, "A central axis algorithm for 3-D bronchial tree structures," in *Proc. Int. Symp. Computer Vision*, vol. 44, Nov. 1995, pp. 259–264.

[34] Y. Masutani, T. Schiemann, and K. H. Höhne, "Vascular shape segmentation and structure extraction using a shape-based region-growing model," in *Proc. Medical Image Analysis and Computer Assisted Intervention (MICCAI)*, Oct. 1998, pp. 1242–1249.

[35] T. Deschamps and L. D. Cohen, "Fast extraction of minimal paths in 3-D images and applications to virtual endoscopy," *Med. Image Anal.*, vol. 5, pp. 281–289, 2001.

[36] C. I. Fetita and F. Prêteux, "CT data-driven 3-D airway model synthesis," in *Proc. World Multiconf. Systemics, Cybernetics, and Informatics*, July 2001, pp. 111–116.

[37] T. Schlathölter, C. Lorenz, I. C. Carlsen, S. Renisch, and T. Deschamps, "Simultaneous segmentation and tree reconstruction of the airways for virtual bronchoscopy," *SPIE Med. Imag. 2002: Physiol. Function from Multidimensional Images*, vol. 4684, Feb. 23–28, 2002.

[38] I. Bitter, A. E. Kaufman, and M. Sato, "Penalized-distance volumetric skeleton algorithm," *IEEE Trans. Visual. Comput. Graph.*, vol. 7, pp. 195–206, July–Sept. 2001.

[39] M. Wan, Z. Liang, Q. Ke, L. Hong, I. Bitter, and A. Kaufman, "Automatic centerline extraction for virtual colonoscopy," *IEEE Trans. Med. Imag.*, vol. 21, pp. 1450–1460, Dec. 2002.

[40] T. Fujii, H. Asakura, H. Emoto, N. Sugou, T. Mito, and I. Shibata, "Automatic path searching for minimally invasive neurosurgical planning," *SPIE Med. Imag. 2002: Physiol. Function from Multidimensional Images*, vol. 4681, Feb. 23–28, 2002.

[41] J. Williams and L. Wolff, "Analysis of the pulmonary vascular tree using differential geometry based vector fields," *Comput. Vis. Image Understanding*, vol. 65, no. 2, pp. 226–236, Feb. 1997.

[42] K. Shoemake, "Animating rotation with quaternion curves," in *Proc. ACM SIGGRAPH*, vol. 19, July 1985, pp. 245–254.

[43] J. Morrison, "Quaternion interpolation with extra spins," in *Graphics Gems*. New York: Academic, 1992, vol. III, pp. 96–97.

[44] P. K. Saha, B. B. Chaudhuri, and D. D. Majumder, "Topology preservation in 3-D digital space," *Pattern Recogn.*, vol. 27, no. 2, pp. 295–300, 1994.

[45] ——, "A new shape preserving parallel thinning algorithm for 3-D digital images," *Pattern Recogn.*, vol. 30, no. 12, pp. 1939–1955, 1997.

[46] Y. Zhou and A. W. Toga, "Efficient skeletonization of volumetric objects," *IEEE Trans. Visual. Comput.. Graphics*, vol. 5, pp. 196–209, July–Sept. 1999.

[47] H. Shikata, "Geometrical analyzes of tree structure in three-dimensional images," Ph.D. thesis, Osaka Univ., Osaka, Japan, Jan. 2002.

[48] G. Borgefors, "Distance transforms in arbitrary dimensions," *Comput. Vis., Graphics Image Processing*, vol. 27, pp. 321–345, 1984.

[49] Y. F. Tsao and K. S. Fu, "A parallel thinning algorithm for 3-D pictures," *Comput. Graphics Image Processing.*, vol. 17, no. 3, pp. 315–331, 1981.

[50] J. Tshirren, E. A. Hoffman, G. McLennan, and M. Sonka, "Branchpoint labeling and matching in human airway trees," *SPIE Med. Imag. 2003: Physiology and Function—Methods, Systems, and Applications*, vol. 5031, 2003.

[51] S. Wan, E. Ritman, and W. Higgins, "Multi-generational analysis and visualization of the vascular tree in 3-D micro-CT images," *Comput. Biol. Med.*, vol. 32, no. 2, pp. 55–71, Feb. 2002.

[52] K. C. Yu, E. L. Ritman, A. P. Kiraly, S. W. Wan, M. Zamir, and W. E. Higgins, "Toward reliable multi-generational analysis of anatomical trees," in *SPIE Med. Imag. 2003: Physiology and Function—Methods, Systems, and Applications*, vol. 5031, A. Clough and A. Amini, Eds., 2003, pp. 178–186.

[53] W. E. Higgins, R. A. Karwoski, W. J. T. Spyra, and E. L. Ritman, "System for analyzing true three-dimensional angiograms," *IEEE Trans. Med. Imag.*, vol. 15, pp. 377–385, June 1996.

[54] U. Shani and D. H. Ballard, "Splines as embeddings for generalized cylinders," *CVGIP*, vol. 27, pp. 129–156, 1984.

[55] D. F. Rogers and A. J. Adams, *Mathematical Elements for Computer Graphics*. New York: McGraw-Hill, 1990.

[56] H. Kitaoka, B. Suki, and R. Takaki, "A three-dimensional model of the human airway tree," *J. Appl. Physiol.*, vol. 87, no. 6, pp. 2207–2217, July 1999.

[57] J. Z. Turlington and W. E. Higgins, "New techniques for efficient sliding thin-slab volume visualization," *IEEE Trans. Med. Imag.*, vol. 20, pp. 823–835, Aug. 2001.

[58] J. P. Helferty, C. Zhang, G. McLennan, and W. E. Higgins, "Videoendoscopic distortion correction and its application to virtual guidance of endoscopy," *IEEE Trans. Med. Imag.*, vol. 20, pp. 605–617, July 2001.

[59] J. P. Helferty and W. E. Higgins, "Technique for registering 3-D virtual CT images to endoscopic video," in *Proc. IEEE Int. Conf. Image Processing 2001*, Oct. 7–10, 2001, pp. 893–896.

[60] W. Higgins, J. Helferty, A. Kiraly, J. Turlington, A. Sherbondy, E. Hoffman, and G. McLennan, "Live guidance of mediastinal lymph node biopsy using virtual bronchoscopy," presented at the Radiologic Soc. North America (RSNA) 2002, Chicago, IL, Nov. 2002.

[61] K. Thomas, J. Helferty, W. Higgins, E. Hoffman, S. Ferguson, A. Delsing, J. Cook-Granroth, K. Wolf, A. Kiraly, and G. McLennan, "Virtual image guidance of mediastinal lymph node fine needle biopsy," *Amer. J. Respiratory Crit. Care*, vol. 165, no. 8, p. A142, Apr. 2002.

[62] S. Ferguson, J. Helferty, W. Higgins, E. Hoffman, J. Reinhardt, K. Thomas, A. Delsing, J. Cook-Granroth, A. Ross, K. Wolf, J. Turlington, and G. McLennan, "Virtual endoscopic guidance for the management of major airway obstruction," *Amer. J. Respiratory Crit. Care*, vol. 165, no. 8, p. A142, Apr. 2002.

[63] W. Higgins, S. Ferguson, K. Thomas, J. Helferty, A. Kiraly, A. Sherbondy, J. Turlington, E. Hoffman, and G. McLennan, "Progress toward virtual-bronchoscopic guidance of peripheral nodule biopsy," *Amer. J. Respiratory Crit. Care*, vol. 167, no. 7, p. A535, May 2003.

[64] M. Suter, J. Reinhardt, M. Sonka, W. Higgins, E. Hoffman, and G. McLennan, "Three dimensional true color topographical analysis of the pulmonary airways," *Proc. SPIE Medical Imaging 2004: Physiology, Function, and Structure from Medica*, vol. 5369, 2004.

[65] C. Rooney, K. Wolf, and G. McLennan, "Ultrathin bronchoscopy as an adjunct to standard bronchoscopy in the diagnosis of peripheral lung lesions," *Respiration*, vol. 69, no. 1, pp. 63–68, 2002.

[66] A. P. Kiraly, "3-D image analysis and visualization of tubular structures," Ph.D. thesis, Pennsylvania State Univ., University Park, Jan. 2003.